

## Supporting Information

### **Intermolecular proton-coupled electron transfer reconstructs aggregates for near-infrared light-driven hydrogen evolution**

Huimin Bai,<sup>a,c</sup> Jie Wang,<sup>a,c</sup> Jianghong Zhao,<sup>\*a</sup> Hongxia Zhang,<sup>a</sup> Hu Shi,<sup>\*a, b</sup> and Pengju Yang<sup>\*a</sup>

---

a School of Chemistry and Chemical Engineering, Shanxi University, 030006, Taiyuan, China

b Institute of Molecular Science, Shanxi University, Taiyuan 030006, China

c These authors contributed equally to this work

## **Content:**

### **MD simulation and DFT calculation**

**Fig. S1.** (a) MD simulation of AT monomer, (b) AT monomer contact map based on MD simulations.

**Fig. S2.** (a) MD simulation of low aggregated AT, (b) Low aggregated AT contact map based on MD simulations.

**Fig. S3.** (a) MD simulation of high aggregated AT, (b) High aggregated AT contact map based on MD simulations.

**Fig. S4.** Normalized PL spectra of AT with different concentrations.

**Fig. S5.** PL spectra of AT aggregates under long-wavelength excitation.

**Fig. S6.** Calculated HOMO-LUMO gaps of AT dimers.

**Fig. S7.** Calculated HOMO-LUMO gaps of AT trimers.

**Fig. S8.** Calculated HOMO-LUMO gaps of AT tetramers.

**Fig. S9.** The function of reduced density gradient and  $\text{sign}(\lambda_2)\rho$  scatter spectrum for AT aggregates based on a MD simulation.

**Fig. S10.** NTO orbital analysis of AT monomer and aggregates.

**Fig. S11.** Schematic diagram of  $n \rightarrow \pi^*$  electronic transition of a AT dimer aggregate.

**Fig. S12.** Oscillator strengths of AT monomer and aggregates.

**Fig. S13.** Orbital interaction diagram of a AT dimer aggregate.

**Fig. S14.** Orbital interaction diagram of a AT trimer aggregate.

**Fig. S15.** Distance between adjacent AT molecules (b, c) based on MD simulation (a).

**Fig. S16.** Distance distributions between adjacent AT molecules based on S15.

**Fig. S17.** RGB integer of AT aggregates and reconstructed AT aggregates.

**Fig. S18.** Calculated HOMO-LUMO gaps of AT aggregates and reconstructed AT aggregates.

**Fig. S19.**  $^1\text{H-NMR}$  spectra (in  $\text{DMSO-d}_6$ ) of AT aggregates.

**Fig. S20.**  $^1\text{H-NMR}$  spectra (in  $\text{DMSO-d}_6$ ) of reconstructed AT aggregates.

**Fig. S21.** IR spectra of AT aggregates and reconstructed AT aggregates.

**Fig. S22.** Electrostatic potential distribution for reconstructed AT aggregates.

**Fig. S23.** Exciton binding energies of AT aggregates and reconstructed AT aggregates.

**Fig. S24.** Distribution of electrostatic potential and calculated dipole moments for AT aggregates and reconstructed AT aggregates.

**Fig. S25.** Hole-electron analysis of AT aggregates and reconstructed AT aggregates.

**Fig. S26.** Mott-Schottky plot of reconstructed AT aggregates.

**Fig. S27.** The color change of the reconstructed AT aggregates after 48 hours test.

**Fig. S28.** UV-vis absorption spectra of the reconstructed AT aggregates after 48 hours test.

**Fig. S29.** Hydrogen-bonded interactions between the reconstructed AT aggregates and L-A.

**Fig. S30.** UV-vis absorption spectra of reconstructed AT aggregates and reconstructed AT aggregates with L-A.

**Fig. S31.** Calculated HOMO-LUMO gaps of reconstructed AT aggregates and reconstructed AT aggregates with L-A.

**Fig. S32.** Orbital interaction diagram of reconstructed AT aggregates (dimer) and L-A.

**Fig. S33.** Hydrogen production performance of reconstructed AT aggregates with L-A under visible and red-light irradiation (500, 530, 590, and 610 nm).

**Fig. S34.** Hydrogen production performance of reconstructed AT aggregates with L-A under 500 nm irradiation.

**Fig. S35.** PL spectra of reconstructed AT aggregates with different aggregation degrees.

**Fig. S36.** Photocatalytic performances of reconstructed AT aggregates with different concentrations.

**Table S1.** Fitting parameters of time-resolved PL lifetime of AT aggregates and reconstructed AT aggregates.

**Table S2.** Fitting parameters of time-resolved PL lifetime of reconstructed AT aggregates, reconstructed AT aggregates 2 and 3.

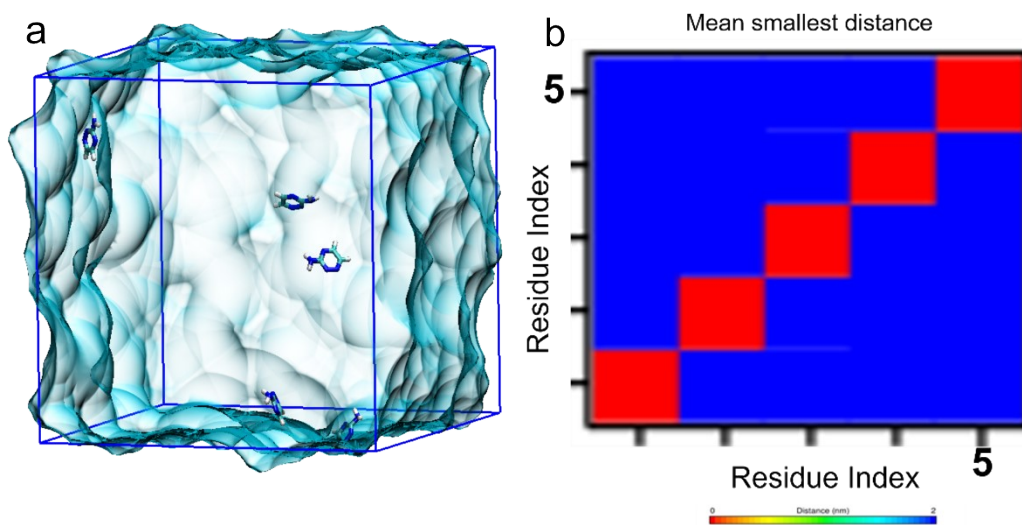
**Table S3.** Comparison of hydrogen production activities with state-of-the-art photocatalysts under NIR light.

**Supplementary references**

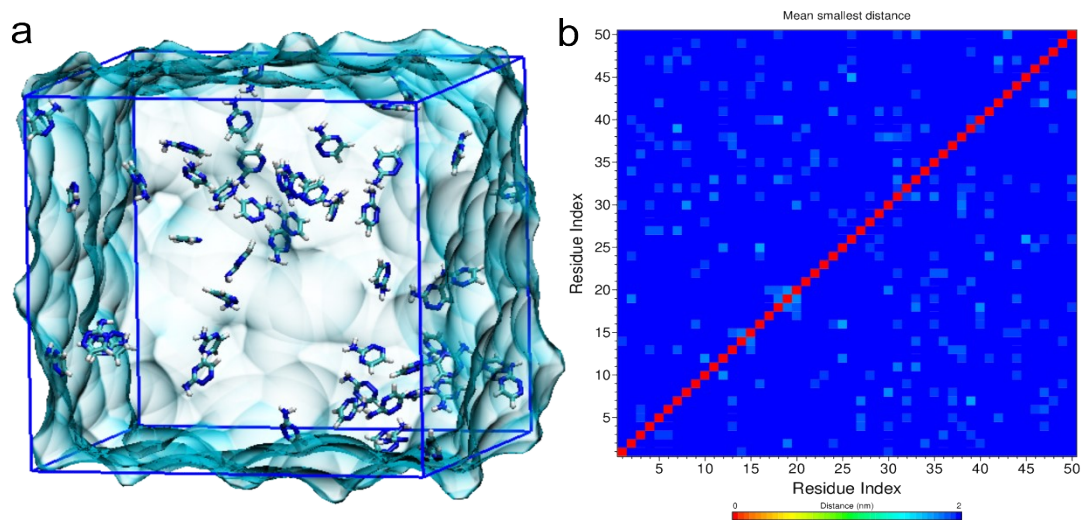
**MD simulation:** MD simulations were performed using the Amber 18 and GROMACS 4.6.7 packages<sup>1</sup> with amber gaff force field for AT molecules<sup>2</sup> and amber14SB force field for the explicit TIP3P.<sup>3</sup> The simulation parameters of AT molecule were derived from Gaussian 09 with B3LYP/6-31G\* level. During the MD simulations, we used the SHAKE<sup>4</sup> method to restrict bonds, including H-bonding. During system modeling, the solute molecules were added into a cubic box of  $5 \times 5 \times 5 \text{ nm}^3$ , and then the solvent molecules were used to fill the box.<sup>5</sup> The particle mesh Ewald summation method was used to describe long-range electrostatics.<sup>6</sup> The cutoff distance is 1.0 nm for nonbonded interactions. The Langevin thermostat and Berendsen barostat were used for temperature and pressure control. In the current study, a 200 ns MD trajectory was collected in each system. After the equilibration checking, only the final equilibrated 50 ns trajectory was used for further analysis.

**DFT calculation:** All calculations were completed by Gaussian 09 software. Density functional theory (DFT) was used to optimize the geometric structures on ground-state properties of AT and reconstructed AT with the B3LYP functional method in combination with the 6-31G\* basis set,<sup>7</sup> while time-dependent DFT (TD-DFT, the same calculation method and basis set) was used to calculate the excited-state properties of AT and reconstructed AT aggregates. The convergence accuracy of SCF reached the default convergence standard. At the same time, the geometric configuration, HOMO-LUMO energy gap and excited-state orbital distribution of AT and reconstructed AT aggregates were analyzed and studied. The electrostatic potential and isosurface maps of various orbitals were exported and visualized with Multiwfn 3.8<sup>8</sup> and VMD

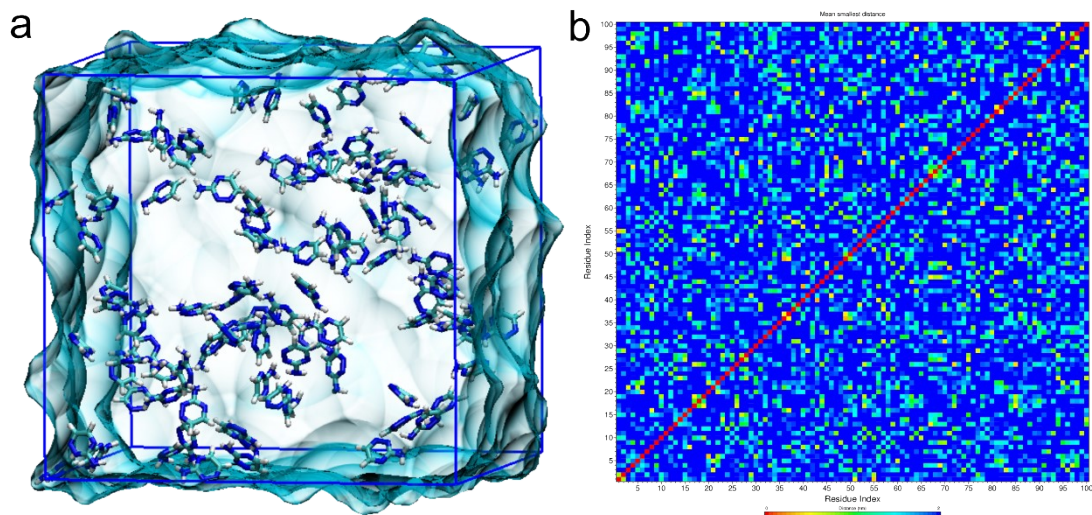
### 1.9.3 software.<sup>9</sup>



**Fig. S1.** (a) MD simulation of AT monomer, (b) AT monomer contact map based on MD simulations.

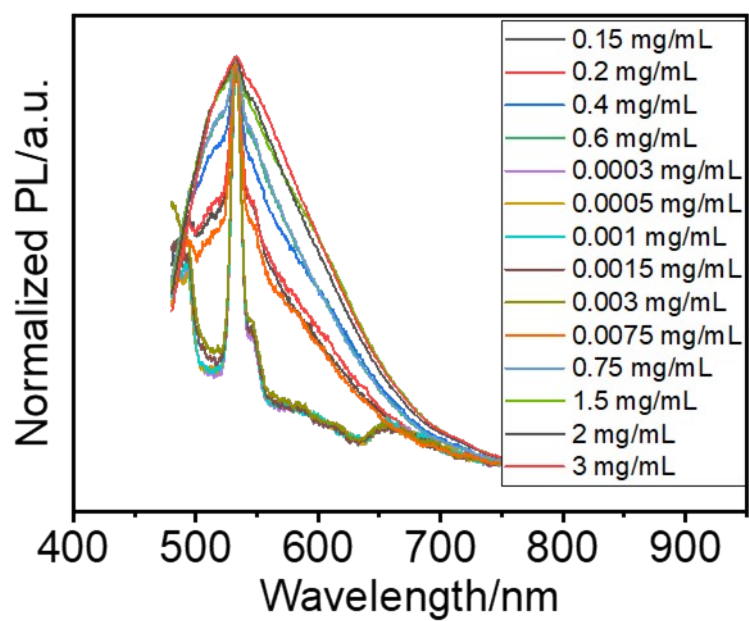


**Fig. S2.** (a) MD simulation of low aggregated AT, (b) Low aggregated AT contact map based on MD simulations.

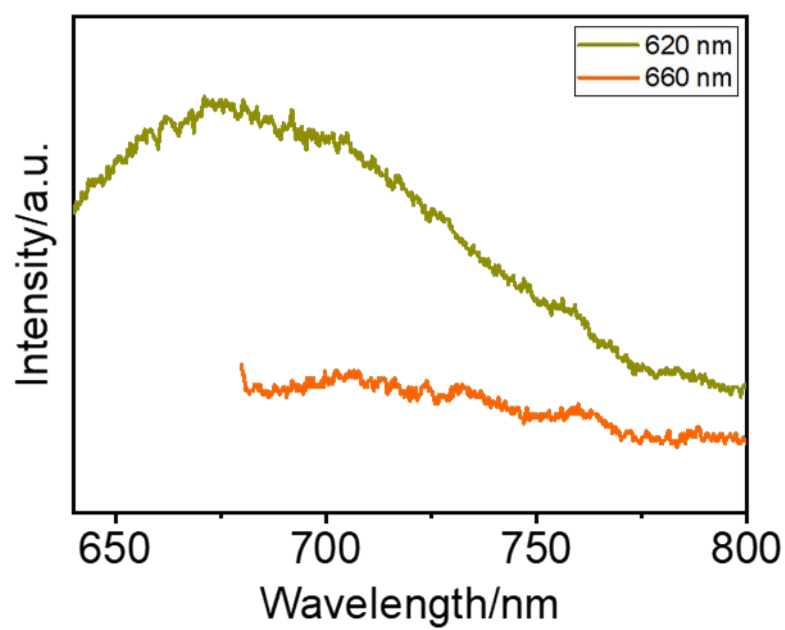


**Fig. S3.** (a) MD simulation of high aggregated AT, (b) High aggregated AT contact map based on MD simulations.





**Fig. S4.** Normalized PL spectra of AT with different concentrations.



**Fig. S5.** PL spectra of AT aggregates under long-wavelength excitation.

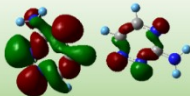
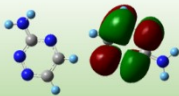
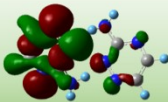
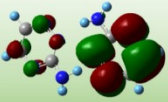
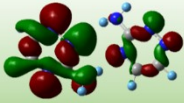
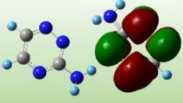
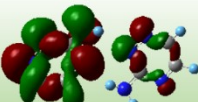
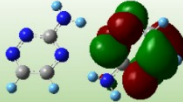
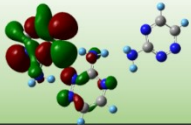
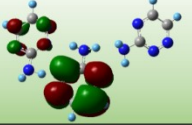
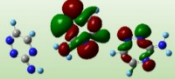
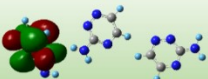
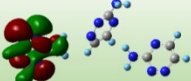
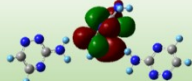
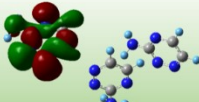
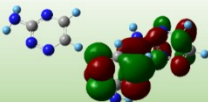
2	HOMO	LUMO	E <sub>g</sub>
Dimer			4.29 eV
Dimer			4.22 eV
Dimer			4.12 eV
Dimer			3.95 eV

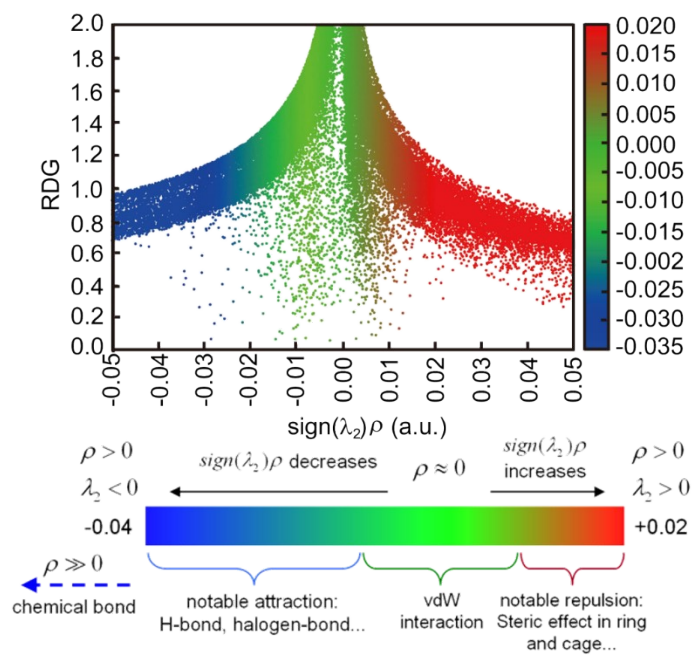
Fig. S6. Calculated HOMO-LUMO gaps of AT dimers.

2	HOMO	LUMO	E <sub>g</sub>
Trimer			4.24 eV
Trimer			4.13 eV
Trimer			4.09 eV
Trimer			3.96 eV

**Fig. S7.** Calculated HOMO-LUMO gaps of AT trimers.

2	HOMO	LUMO	E <sub>g</sub>
Tetramer			3.92 eV
Tetramer			3.53 eV
Tetramer			3.38 eV
Tetramer			3.05 eV

**Fig. S8.** Calculated HOMO-LUMO gaps of AT tetramers.



**Fig. S9.** The function of reduced density gradient and  $\text{sign}(\lambda_2)\rho$  scatter spectrum for AT aggregates based on a MD simulation.

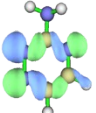
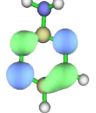
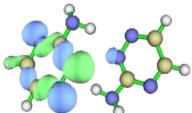
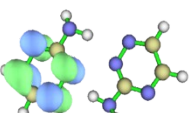
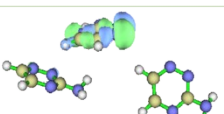
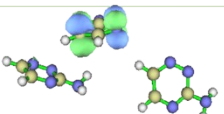
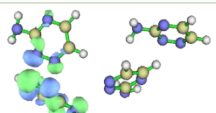
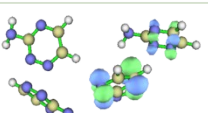
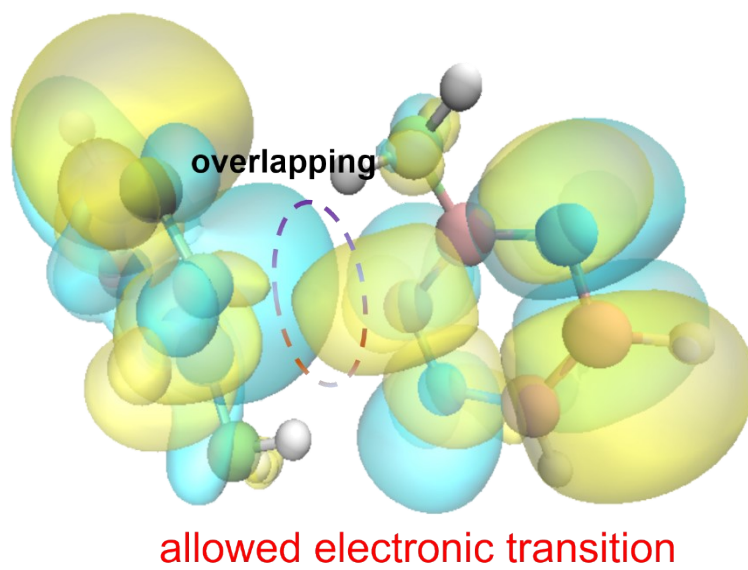
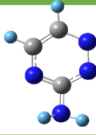
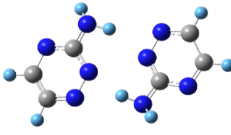
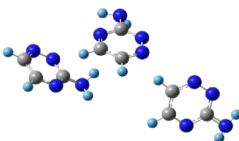
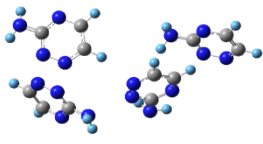
	HOMO	LUMO	Transition type
Monomer			$n \rightarrow \pi^*$
Dimer			$n \rightarrow \pi^*$
Trimer			$n \rightarrow \pi^*$
Tetramer			$n \rightarrow \pi^*$

Fig. S10. NTO orbital analysis of AT monomer and aggregates.



**Fig. S11.** Schematic diagram of  $n \rightarrow \pi^*$  electronic transition of a AT dimer aggregate.



Asymmetric structure	$f$ (oscillator)
n=1 	0.0054
n=2 	0.0099
n=3 	0.0103
n=4 	0.0206

**Fig. S12.** Oscillator strengths of AT monomer and aggregates.

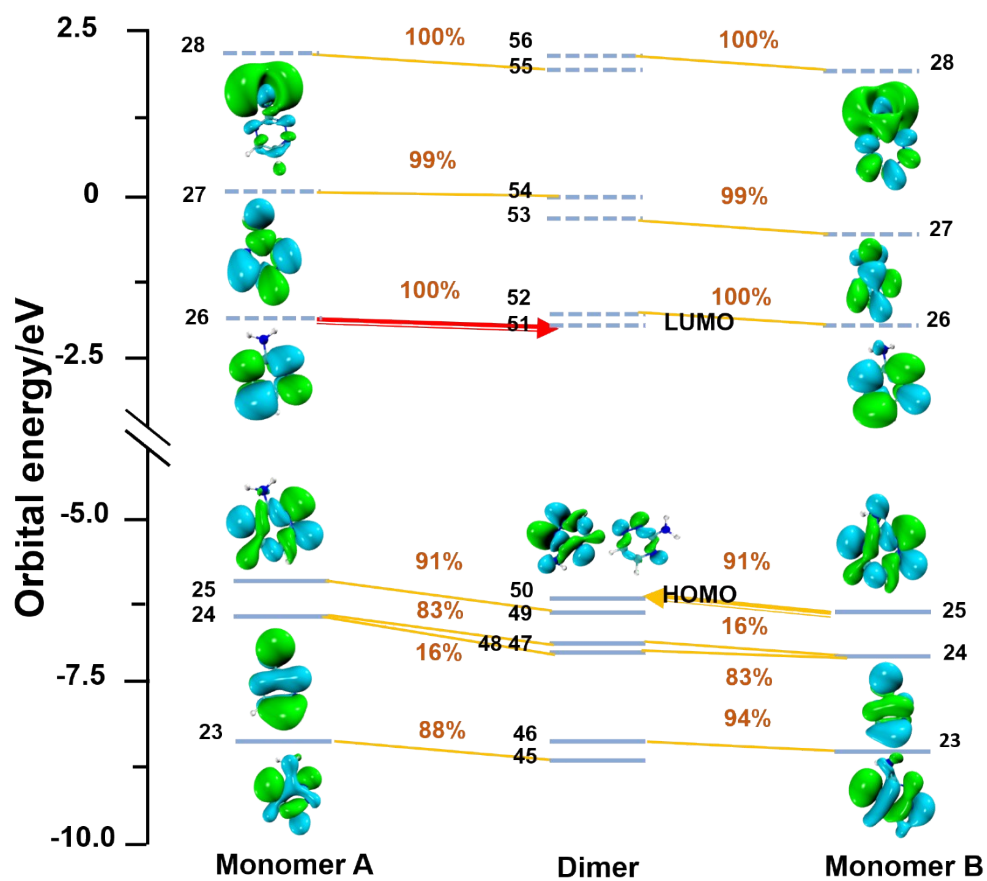


Fig. S13. Orbital interaction diagram of a AT dimer aggregate.

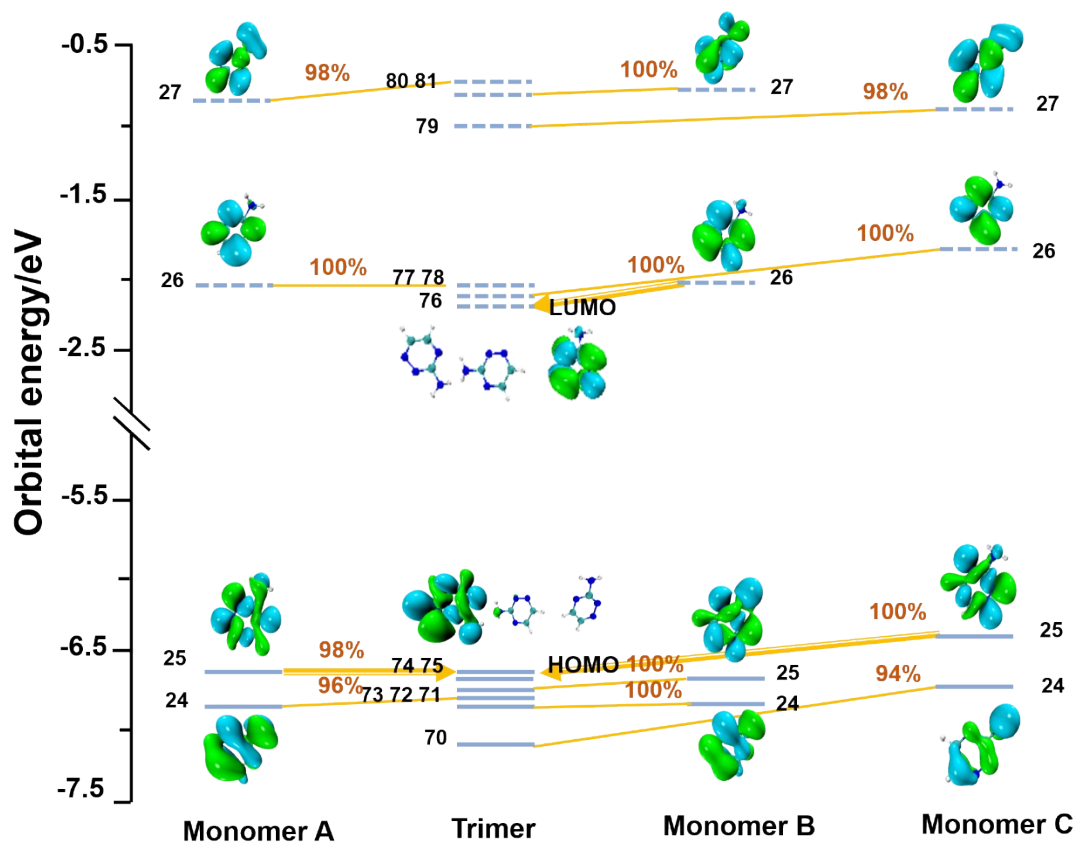
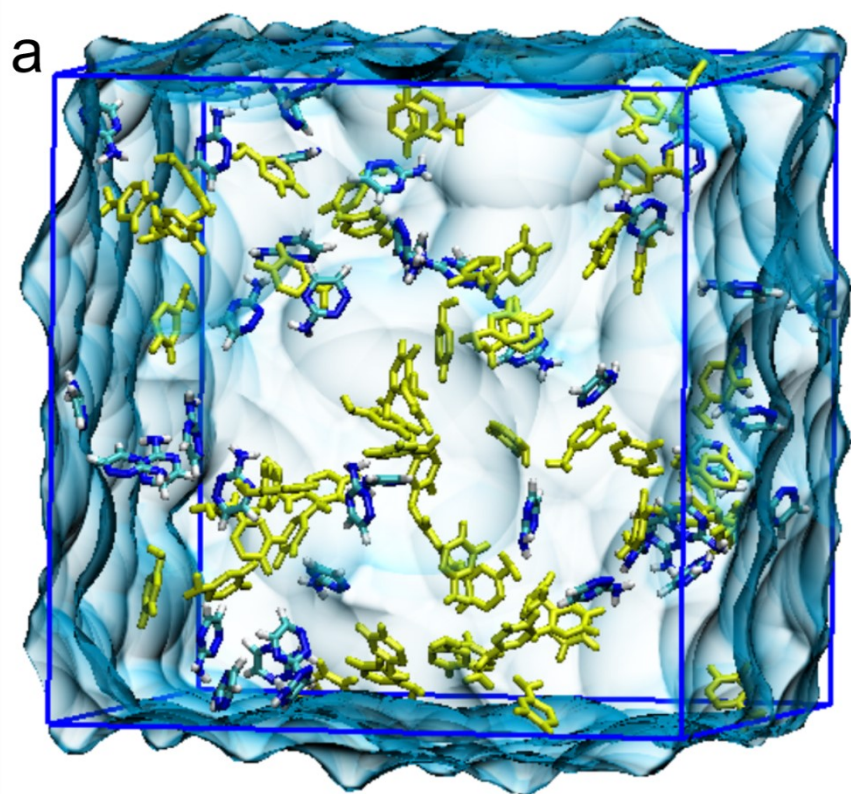
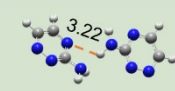
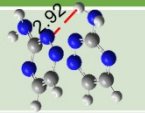
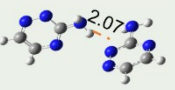
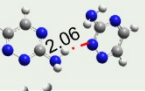
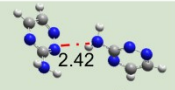
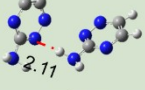

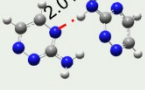
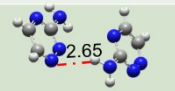
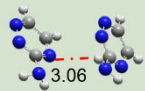
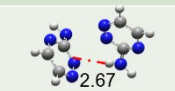
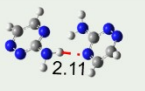
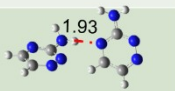
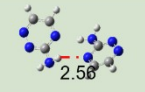
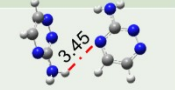
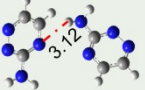
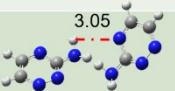
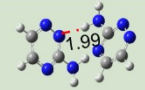
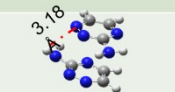
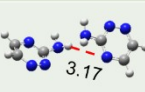

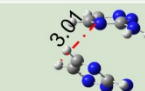
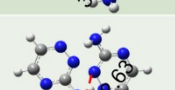
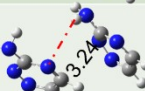
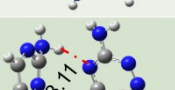
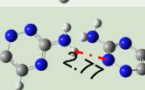
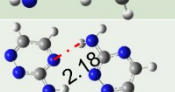
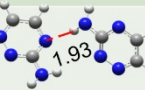
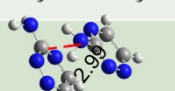
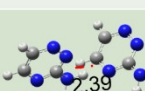


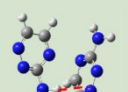
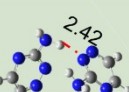


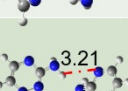
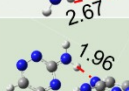

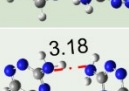
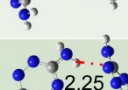
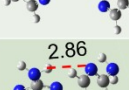
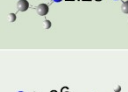
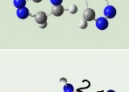
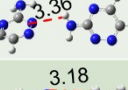
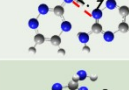
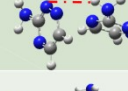


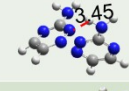
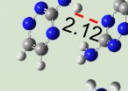


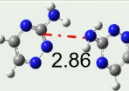
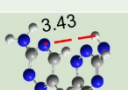
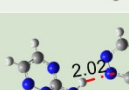
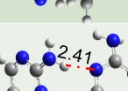
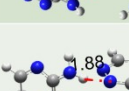
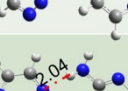
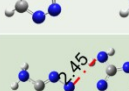
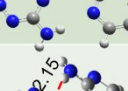
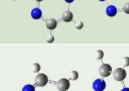
Fig. S14. Orbital interaction diagram of a AT trimer aggregate.



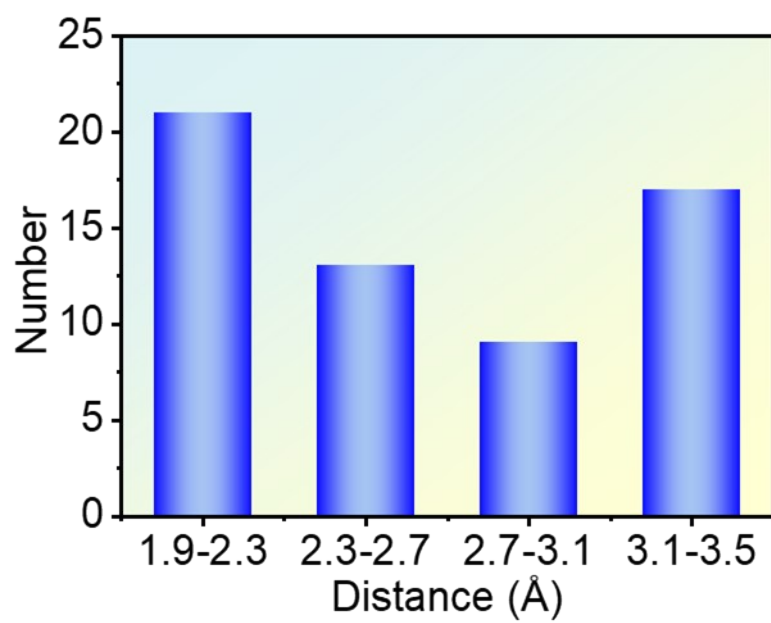
**b**

Atomic number	Distance (Å)	Atomic number	Distance (Å)
3-25		8-97	
7-31		3-98	
12-68		23-100	
9-72		9-88	
33-93		46-77	
48-100		77-99	
52-53		84-15	
59-100		86-85	
61-58		90-97	
73-8		99-46	
58-86		49-37	
2-29		26-72	
73-66		33-80	
69-4		7-69	
44-18		47-25	

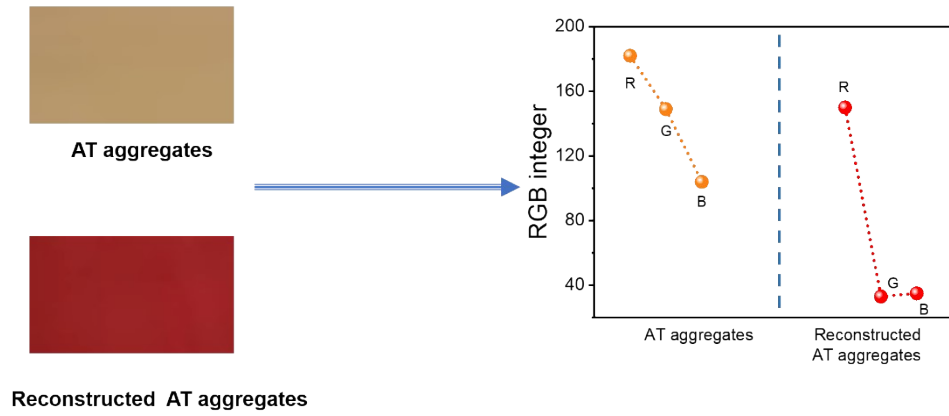
**C**

Atomic number	Distance (Å)	Atomic number	Distance (Å)
14-50		47-81	
33-93		48-100	
34-9		53-2	
34-38		62-81	
37-50		66-68	
66-86		91-15	
72-9		97-19	
69-68		93-18	
77-99		97-39	
84-57		99-11	
61-78		41-77	
85-53		100-94	
47-71		84-87	
60-5		31-57	
64-93		40-43	

**Fig. S15.** Distance between adjacent AT molecules (b, c) based on MD simulation (a).

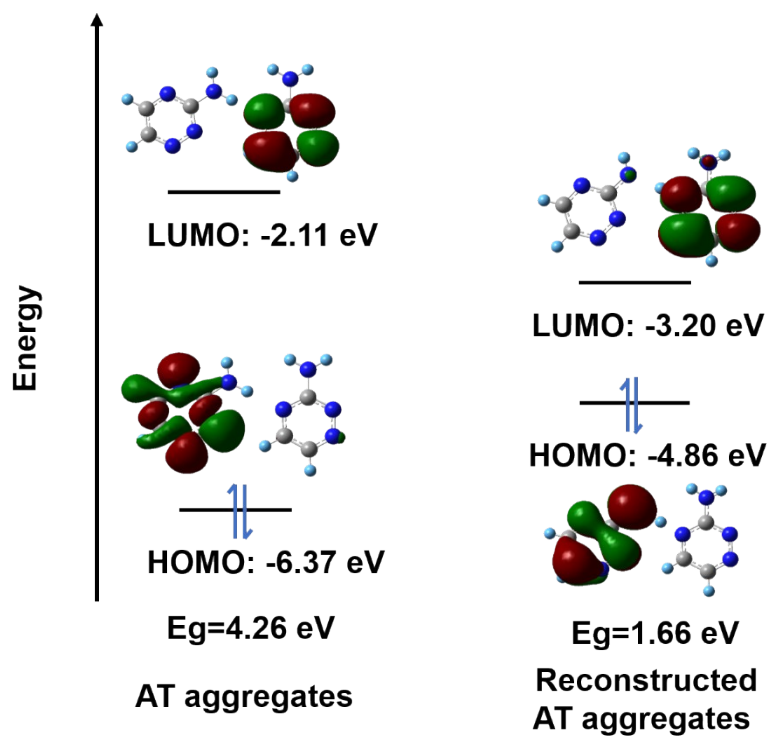


**Fig. S16.** Distance distributions between adjacent AT molecules based on S15.

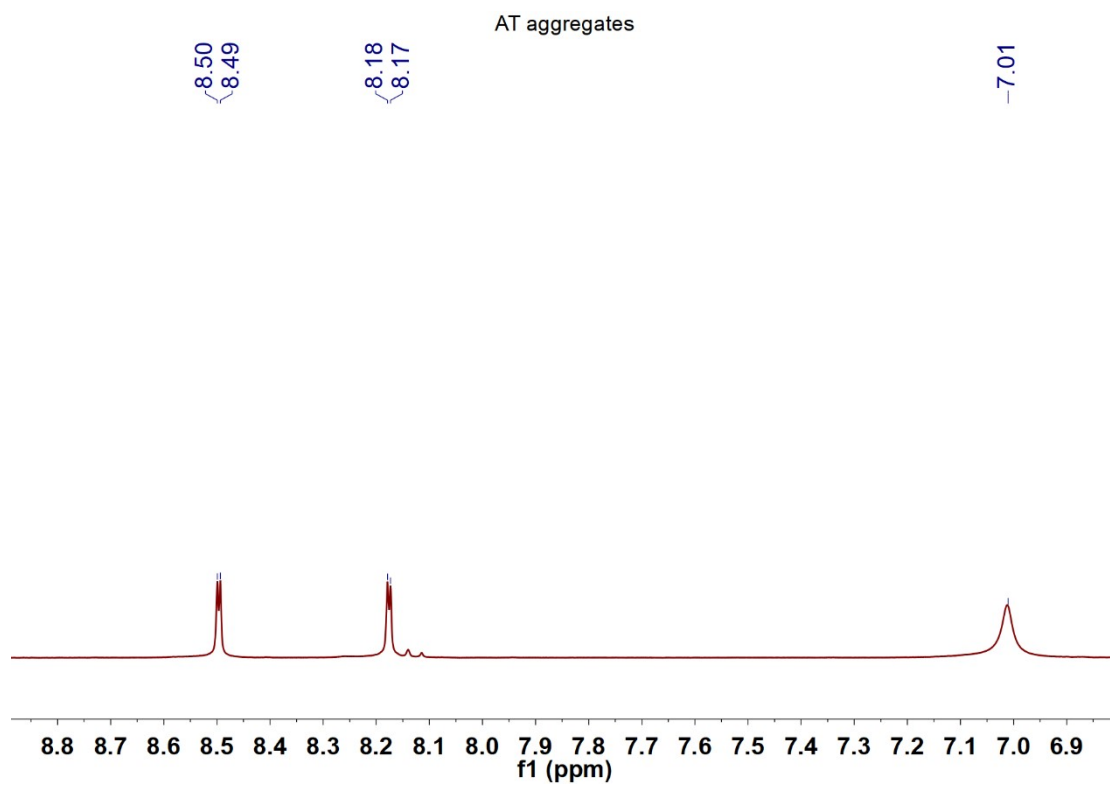


**Fig. S17.** RGB integer of AT aggregates and reconstructed AT aggregates (RGB represents the color of the red, green, and blue channels).

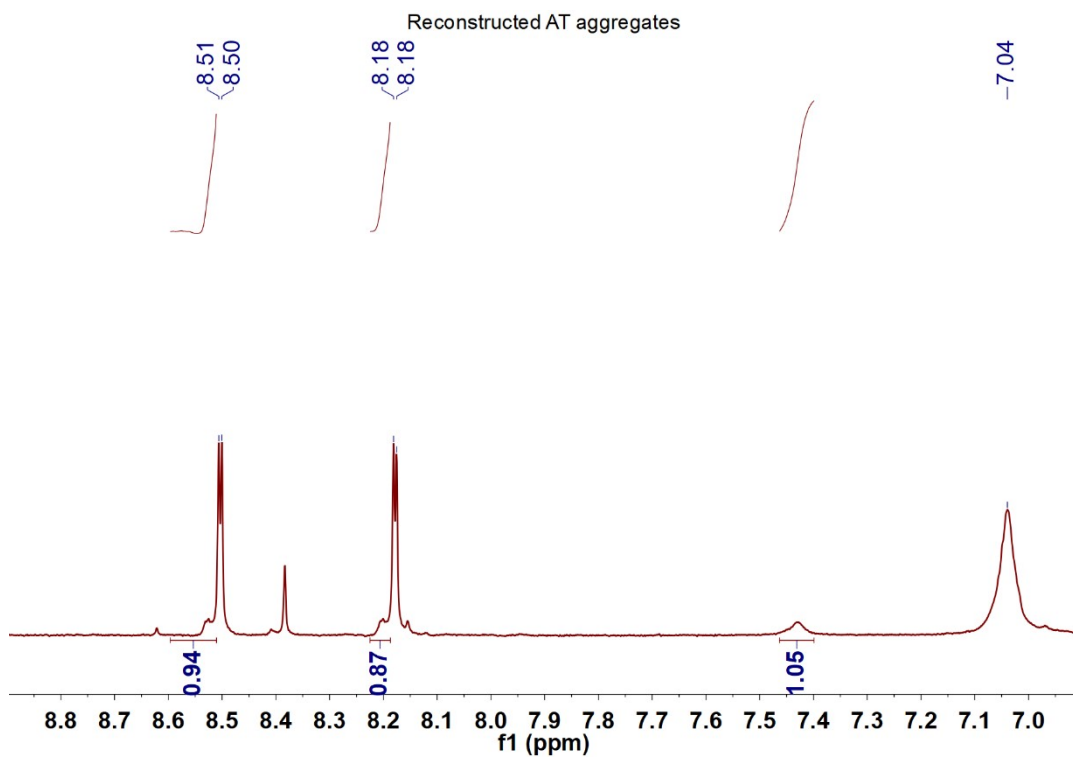




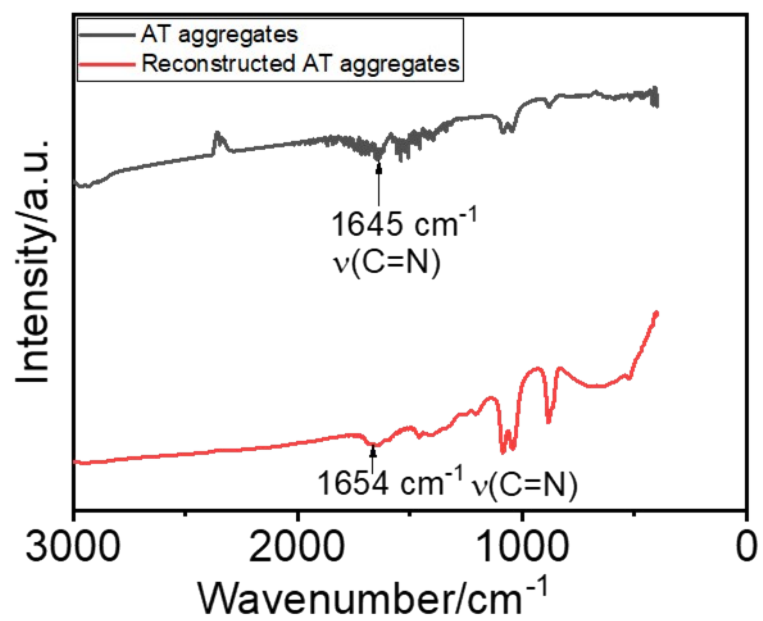
**Fig. S18.** Calculated HOMO-LUMO gaps of AT aggregates and reconstructed AT aggregates.



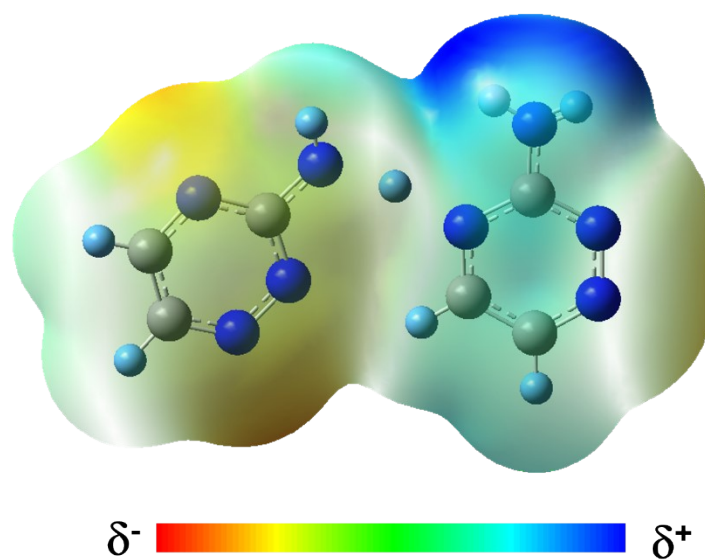
**Fig. S19.**  $^1\text{H-NMR}$  spectra (in  $\text{DMSO-d}_6$ ) of AT aggregates.



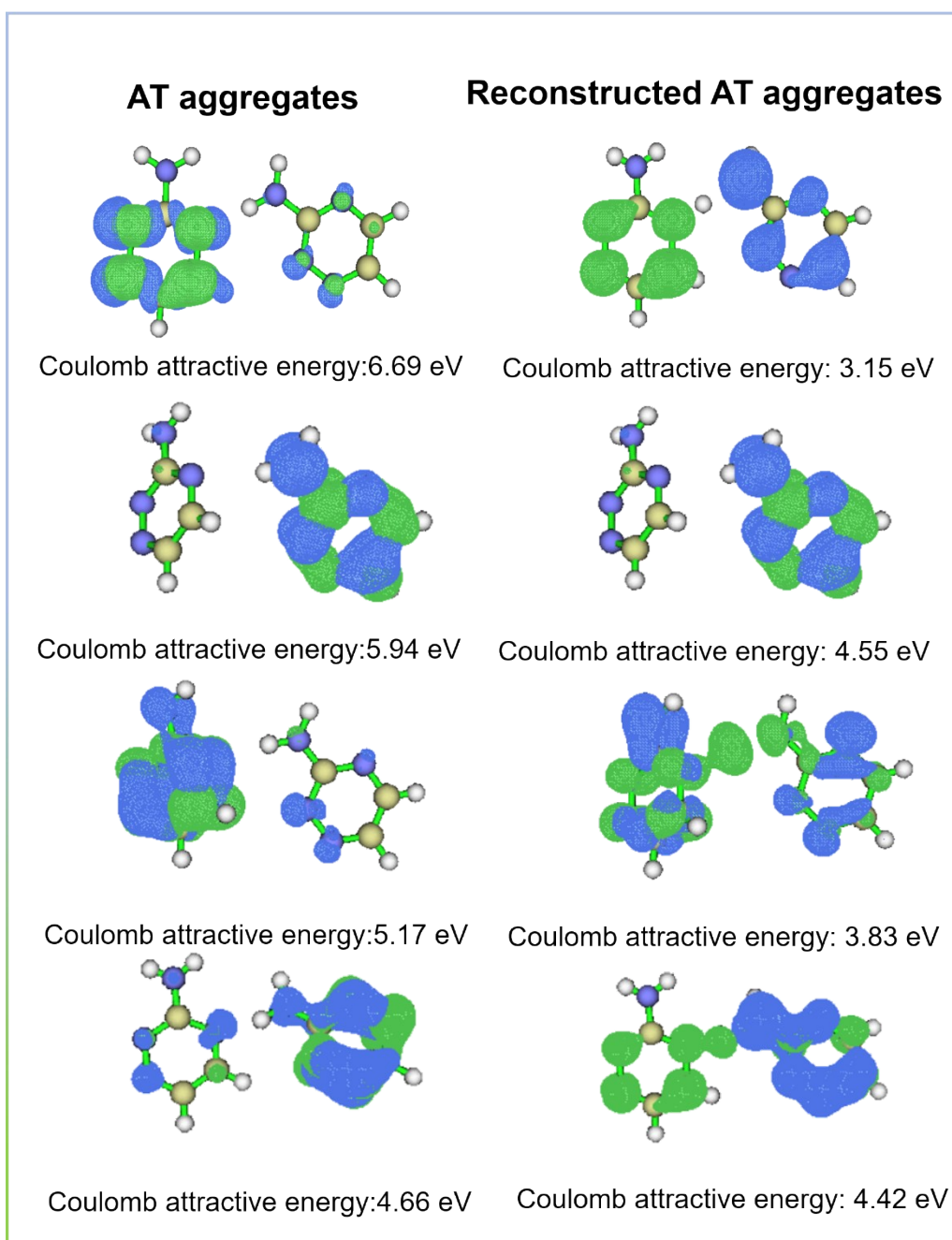
**Fig. S20.**  $^1\text{H}$ -NMR spectra (in  $\text{DMSO-d}_6$ ) of reconstructed AT aggregates.



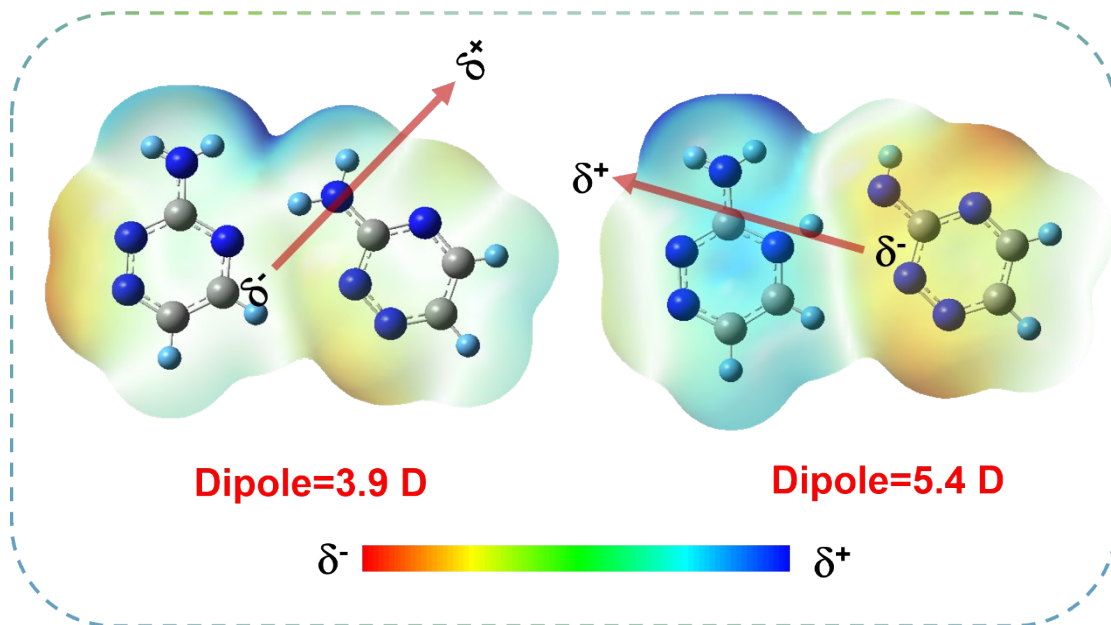
**Fig. S21.** FTIR spectra of AT aggregates and reconstructed AT aggregates.



**Fig. S22.** Electrostatic potential distribution for reconstructed AT aggregates.



**Fig. S23.** Exciton binding energies of AT aggregates and reconstructed AT aggregates.

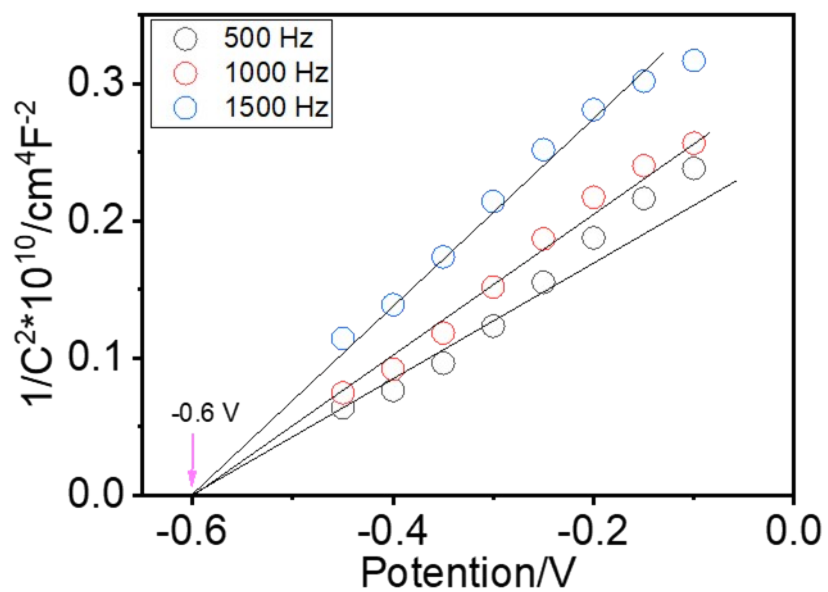


**Fig. S24.** Distribution of electrostatic potential and calculated dipole moments for AT aggregates and reconstructed AT aggregates.

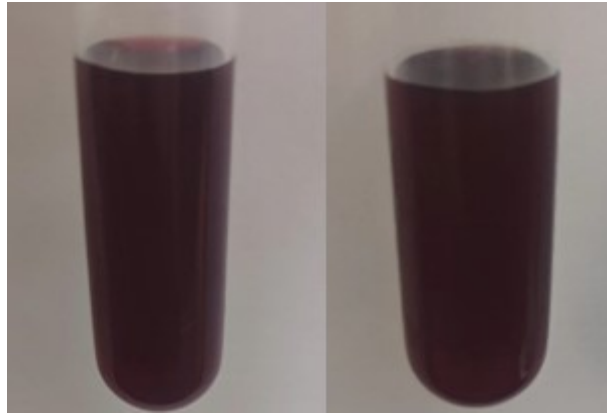
	<b>D</b> (Å)	<b>S<sub>r</sub></b> (a.u.)	<b>S<sub>m</sub></b> (a.u.)	<b>H</b> (Å)	<b>HDI</b>	<b>EDI</b>
<b>AT aggregates</b>	0.506	0.745	0.526	2.192	9.30	9.41
<b>Reconstructed AT aggregates</b>	0.591	0.686	0.470	3.334	7.06	6.75

**Fig. S25.** Hole-electron analysis of AT aggregates and reconstructed AT aggregates.

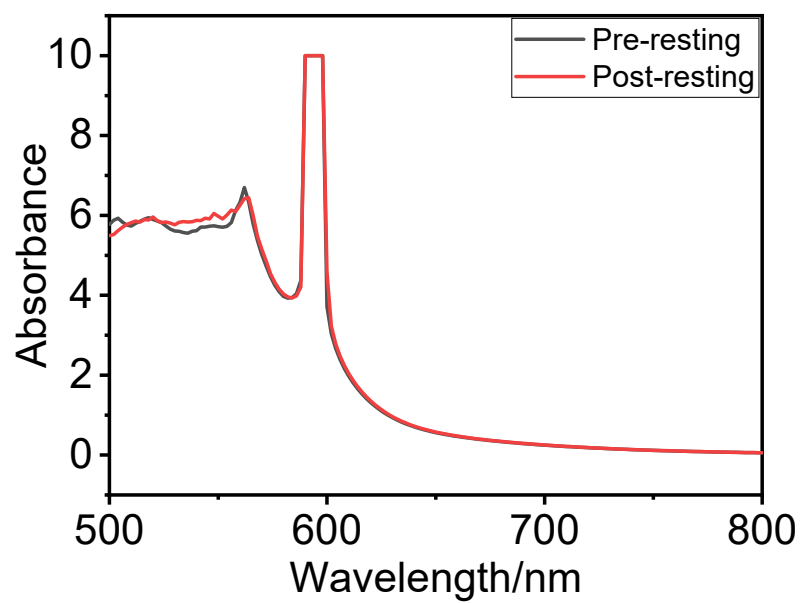




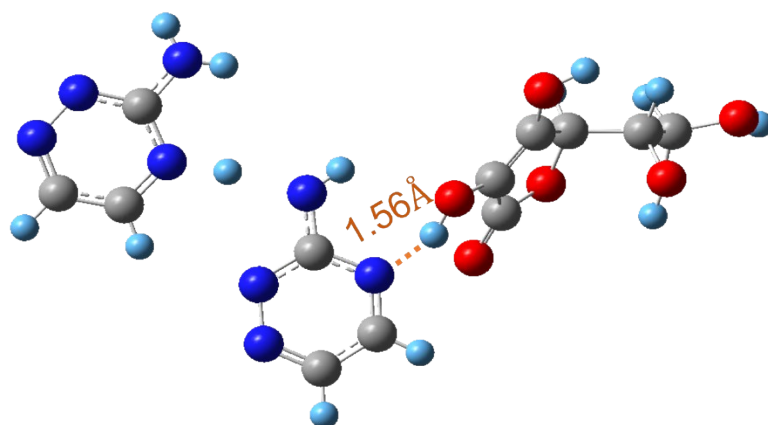
**Fig. S26.** Mott-Schottky plot of reconstructed AT aggregates. (As a rule of thumb, the difference between the CB and the FB is  $\sim 0.2 \text{ V}^{[10]}$ . The conduction band (CB) of reconstructed AT aggregates are estimated to be  $-0.56 \text{ V}$  (vs NHE pH = 7)).



**Fig. S27.** The color change of the reconstructed AT aggregates after 48 hours test.

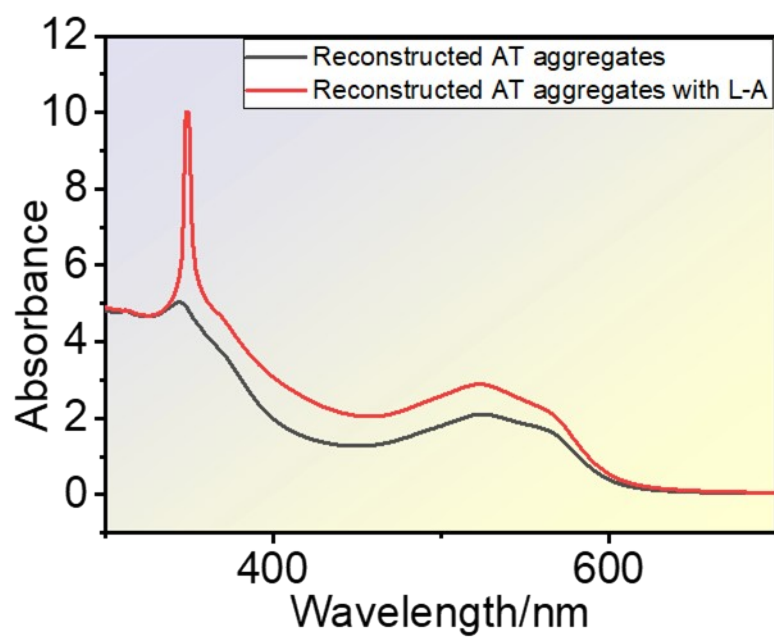


**Fig. S28.** UV-vis absorption spectra of the reconstructed AT aggregates after 48 hours test.

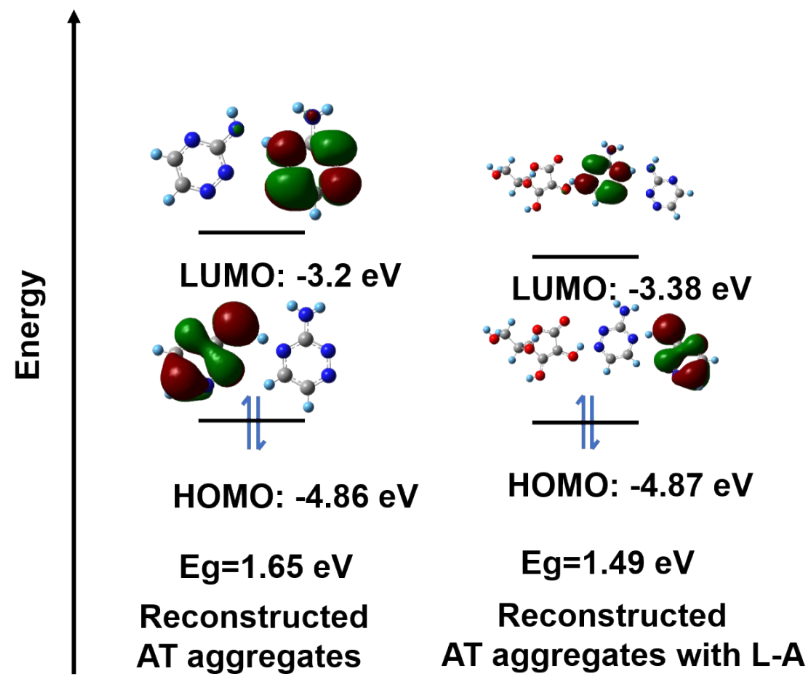


Interaction energy = -8.45 kJ/mol

**Fig. S29.** Hydrogen-bonded interactions between the reconstructed AT aggregates and L-A.



**Fig. S30.** UV-vis absorption spectra of reconstructed AT aggregates and reconstructed AT aggregates with L-A.



**Fig. S31.** Calculated HOMO-LUMO gaps of reconstructed AT aggregates and reconstructed AT aggregates with L-A.

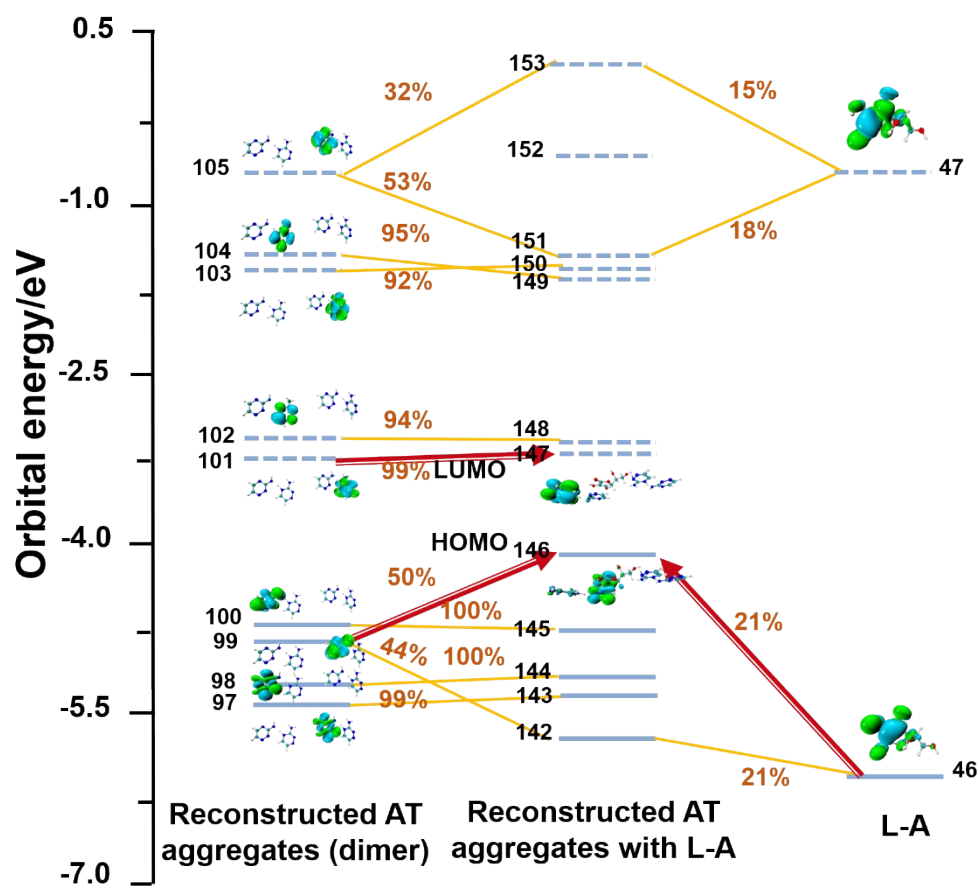
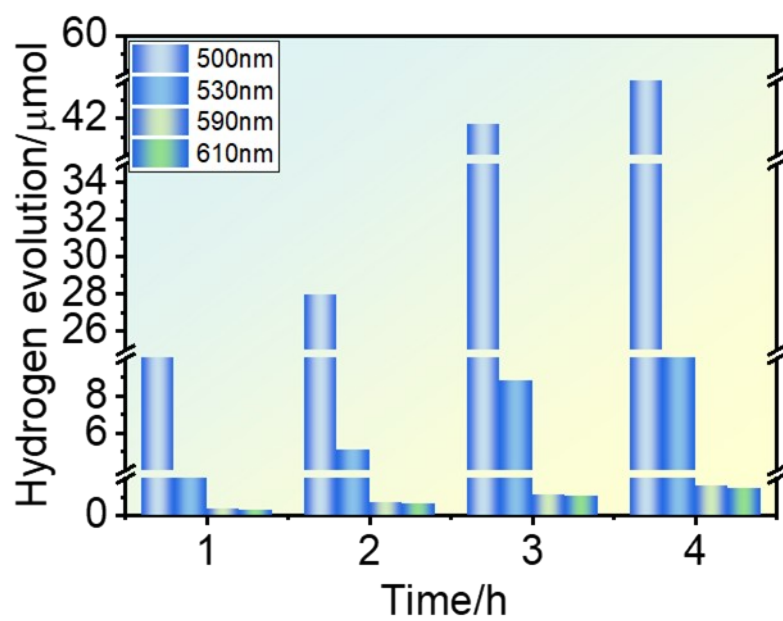
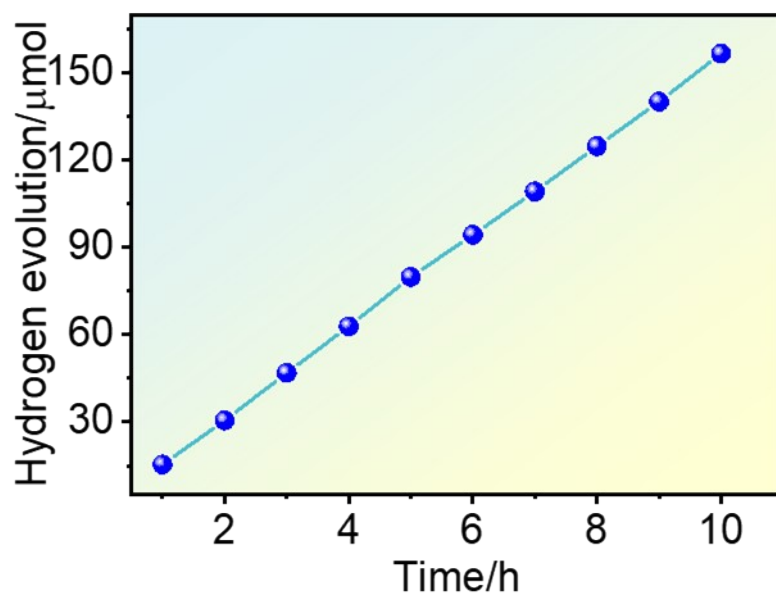


Fig. S32. Orbital interaction diagram of reconstructed AT aggregates (dimer) and L-A.

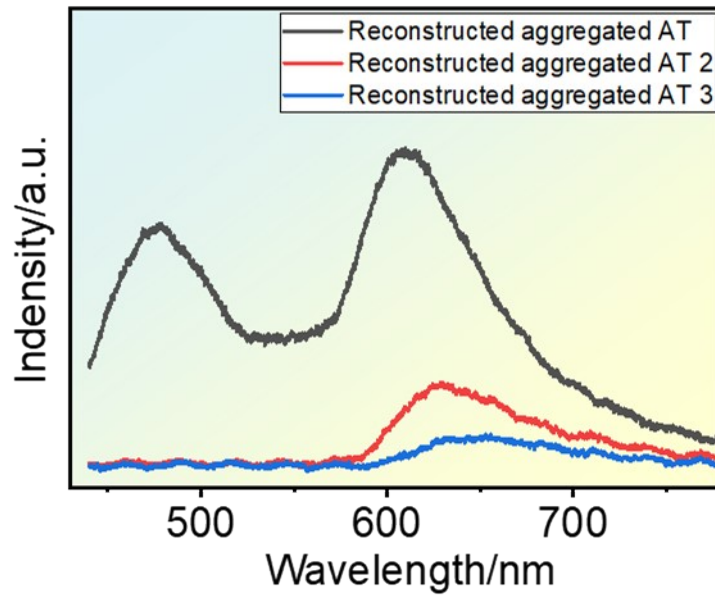


**Fig. S33.** Hydrogen production performance of reconstructed AT aggregates with L-A under visible and red-light irradiation (500, 530, 590, and 610 nm).

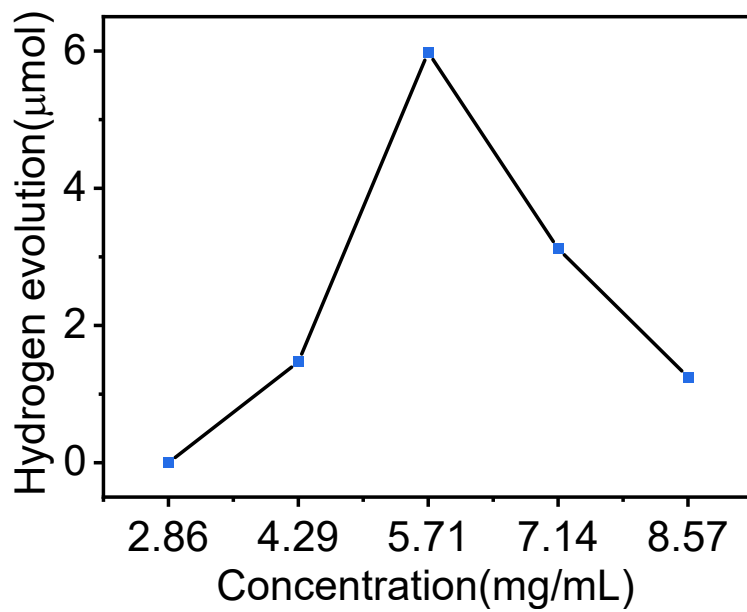




**Fig. S34.** Hydrogen production performance of reconstructed AT aggregates with L-A under 500 nm irradiation.



**Fig. S35.** PL spectra of reconstructed AT aggregates with different aggregation degrees.



**Fig. S36.** Photocatalytic performances of reconstructed AT aggregates with different concentrations (reaction time: 4h; center wavelength: 850 nm; light intensity: 156 mW/cm<sup>2</sup>).

**Table S1.** Fitting parameters of time-resolved PL lifetime of AT aggregates and

reconstructed AT aggregates

samples	$\tau_1/\text{ns}$	$\tau_2/\text{ns}$	$\tau_3/\text{ns}$	$\tau_{\text{ave}}/\text{ns}$
AT aggregates	0.50(28.8%)	3.12(45.8%)	8.27(25.4%)	3.67 ns
Reconstructed AT aggregates	0.52(12.8%)	2.17(28.7%)	6.50(58.5%)	4.50 ns

Note:  $\tau_{\text{ave}} = \frac{A_1 \tau_1^2 + A_2 \tau_2^2 + A_3 \tau_3^2}{A_1 \tau_1 + A_2 \tau_2 + A_3 \tau_3}$

**Table S2.** Fitting parameters of time-resolved PL lifetime of reconstructed AT aggregates, reconstructed AT aggregates 2 and 3

samples	$\tau_1/\text{ns}$	$\tau_2/\text{ns}$	$\tau_3/\text{ns}$	$\tau_{\text{ave}}/\text{ns}$
Reconstructed AT aggregates	0.56(14.9%)	2.48(31.8%)	6.87(53.3%)	4.53 ns
Reconstructed AT aggregates 2	0.57(5.2%)	3.20(56.9%)	9.54(37.9%)	5.46 ns
Reconstructed AT aggregates 3	0.84(18.3%)	4.44(62.2%)	17.01(19.6%)	6.26 ns

Note:  $\tau_{\text{ave}} = \frac{A_1 \tau_1^2 + A_2 \tau_2^2 + A_3 \tau_3^2}{A_1 \tau_1 + A_2 \tau_2 + A_3 \tau_3}$

**Table S3.** Comparison of hydrogen production activities with state-of-the-art photocatalysts under NIR light.

Photocatalysts	Electron donors	QYs/%	Refs.
PM6:2FBP-4F	Ascorbic acid	13.9(808 nm)	11
W <sub>18</sub> O <sub>49</sub> /g-C <sub>3</sub> N <sub>4</sub>	Triethanolamine	0.016(800 nm)	12
Au nanorods/La <sub>2</sub> Ti <sub>2</sub> O <sub>7</sub>	Methanol	0.85(800 nm)	13
BP/TMC	Methanol	1.2(780 nm)	14
BP/g-C <sub>3</sub> N <sub>4</sub>	Methanol	1.1(780 nm)	15
BP/Pt/RGO	Ethylene Diamine Tetraacetic Acid	1.5(780 nm)	16
CdS/Cu <sub>7</sub> S <sub>4</sub>	Na <sub>2</sub> S-Na <sub>2</sub> SO <sub>3</sub>	0.85(800 nm)	17
Amorphous Co <sub>2</sub> B	Triethanolamine	1.15(800 nm) 1.8(1000 nm) 3.8(1100 nm)	18
Pt/CdS/NYF	----	0.008(800 nm)	19
TiO <sub>2</sub> /r-GQDs	----	0.26(850 nm)	20
PA-Ni@PCN	Methanol	2.8(940 nm)	21
Reconstructed AT aggregates	Formic acid	1.23(850 nm)	This work

## Supplementary references

- 1 S. Chaudhury, S. Lyskov, J. J. Gray, *Bioinformatics* 2010, **26**, 689-691.
- 2 V. Hornak, R. Abel, A. Okur, B. Strockbine, A. Roitberg, C. Simmerling, *Proteins* 2006, **65**, 712-725.
- 3 W. Jorgensen, J. Chandrasekhar, J. Madura, R. Impey, M. Klein, *J. Chem. Phys.* 1983, **79**, 926-935.
- 4 S. Miyamoto, P. A. Kollman, *J. Comput. Chem.* 1992, **13**, 952-962.
- 5 P. Eastman, M. S. Friedrichs, J. D. Chodera, R. J. Radmer, C. M. Bruns, J. P. Ku, K. A. Beauchamp, T. J. Lane, L. P. Wang, D. Shukla, T. Tye, M. Houston, T. Stich, C. Klein, M. R. Shirts, V. S. Pande, *J. Chem. Theory Comput.* 2013, **9**, 461-469.
- 6 S. Piana, K. Lindorff-Larsen, David E. Shaw, *Biophysical Journal* 2011, **100**, L47-L49.
- 7 J. Tirado-Rives, W. L. Jorgensen, *J. Chem. Theory Comput.* 2008, **4**, 297-306.
- 8 T. Lu, F. Chen, *J. Comput. Chem.* 2012, **33**, 580-592.
- 9 W. Humphrey, A. Dalke, K. Schulten, *J. Mol. Graph.* 1996, **14**, 33-38.
- 10 N. Hirayama, H. Nakata, H. Wakayama, S. Nishioka, T. Kanazawa, R. Kamata, Y. Ebato, K. Kato, H. Kumagai, A. Yamakata, K. Oka, K. Maeda, *J. Am. Chem. Soc.* 2019, **141**, 17158-17165.
- 11 Z. Zhang, C. Xu, Q. Sun, Y. Zhu, W. Yan, G. Cai, Y. Li, W. Si, X. Lu, W. Xu, Y. Yang, Y. Lin, *Angew. Chem. Int. Ed.* 2024, **63**, e202402343.
- 12 Z. Zhang, J. Huang, Y. Fang, M. Zhang, K. Liu, B. Dong, *Adv. Mater.* 2017, **29**, 1606688.
- 13 X. Cai, M. Zhu, O. A. Elbanna, M. Fujitsuka, S. Kim, L. Mao, J. Zhang, T. Majima, *ACS Catal.* **2018**, **8**, 122-131.
- 14 O. Elbanna, M. Zhu, M. Fujitsuka, T. Majima, *ACS Catal.* 2019, **9**, 3618-3626.
- 15 M. Zhu, S. Kim, L. Mao, M. Fujitsuka, J. Zhang, X. Wang, T. Majima, *J. Am. Chem. Soc.* 2017, **139**, 13234-13242.
- 16 M. Zhu, Y. Osakada, S. Kim, M. Fujitsuka, T. J. A. C. B.-e. Majima, *Appl. Catal. B Environ.* 2017, **217**, 285-292.
- 17 Z. Lian, M. Sakamoto, J. J. M. Vequizo, C. S. K. Ranasinghe, A. Yamakata, T. Nagai, K. Kimoto, Y. Kobayashi, N. Tamai, T. Teranishi, *J. Am. Chem. Soc.* 2019, **141**, 2446-2450.
- 18 J. Tang, T. Zhao, Y. He, R. Guo, W. Pan, H. Zhang, B. Dou, *Renewable Energy* 2024, **222**, 119916.
- 19 W. Gao, B. Tian, W. Zhang, X. Zhang, Y. Wu, G. Lu, *Appl. Catal. B Environ.* 2019, **257**, 117908.
- 20 D. Jia, X. Li, Q. Chi, J. Low, P. Deng, W. Wu, Y. Wang, K. Zhu, W. Li, M. Xu, X. Xu, G. Jia, W. Ye, P. Gao, Y. Xiong, *Research* 2022, **2022**, 9781453.
- 21 Y. Huang, Y. Jian, L. Li, D. Li, Z. Fang, W. Dong, Y. Lu, B. Luo, R. Chen, Y. Yang, M. Chen, W. Shi, *Angew. Chem. Int. Ed.* 2021, **60**, 5245-5249.